

Unraveling the Mechanisms of Zirconium Metal–Organic Frameworks-Based Mixed-Matrix Membranes Preventing Polysulfide Shuttling

Wenqing Lu, Zhenfeng Pang, Aran Lemaire, Fu Liu, Shan Dai, Moisés L. Pinto, Rezan Demir-Cakan, Kong Ooi Tan, Veronique Van Speybroeck, Vanessa Pimenta,* and Christian Serre*


Lithium–sulfur batteries are considered as promising candidates for next-generation energy storage devices for grid applications due to their high theoretical energy density. However, the inevitable shuttle effect of lithium polysulfides and/or dendrite growth of Li metal anodes hinder their commercial viability. Herein, the microporous Zr fumarate metal–organic framework (MOF)-801(Zr) is considered to produce thin ($\approx 15.6 \mu\text{m}$, $\approx 1 \text{ mg cm}^{-2}$) mixed-matrix membranes (MMM) as a novel interlayer for Li–S batteries. It is found that the MOF-801(Zr)/C/PVDF-HFP composite interlayer facilitates Li^+ ions diffusion, and anchors polysulfides while promoting their redox conversion effectively. It is demonstrated that MOF-801 effectively trapped polysulfides at the cathode side, and confirmed for the first time the nature of the interaction between the adsorbed polysulfides and the host framework, through a combination of solid-state nuclear magnetic resonance and molecular dynamics simulations. The incorporation of MOF-801(Zr)/C/PVDF-HFP MMM interlayer results in a notable enhancement in the initial capacity of Li–S batteries up to 1110 mA h g^{-1} . Moreover, even after 50 cycles, a specific capacity of 880 mA h g^{-1} is delivered.

1. Introduction

Lithium–sulfur batteries (Li–S) are considered as one of the most promising next-generation energy storage systems for grid applications due to their high energy density and cost-effectiveness.^[1–6] However, a few drawbacks still limit their commercial application, such as their capacity fading and/or short cycle life due to the shuttle effect of soluble lithium polysulfides.^[7–10] To mitigate this problem, the modification of conventional separators (e.g., glass fiber or Celgard) by including microporous materials has been proposed. Although this strategy has been extensively studied so far, modified separators are usually intrinsically limited, since the cohesion between the rigid functional material and the flexible separator is poor.^[11–13] Another strategy that in principle might overcome this limitation consists of the use of an interlayer, usually a self-standing film, placed between the sulfur cathode and the anode. At present, there are few reports about interlayers,

W. Lu, S. Dai, V. Pimenta, C. Serre
Institut des Matériaux Poreux de Paris
ESPCI Paris, Ecole Normale Supérieure, CNRS, PSL University
75005 Paris, France
E-mail: vanessa.pereira-pimenta@espci.psl.eu;
christian.serre@espci.psl.eu

Z. Pang, K. Ooi Tan
Laboratoire des Biomolécules, LBM
Département de Chimie
École Normale Supérieure, PSL University
Sorbonne Université, CNRS
75005 Paris, France

 The ORCID identification number(s) for the author(s) of this article can be found under <https://doi.org/10.1002/smssc.202300339>.

© 2024 The Authors. Small Science published by Wiley-VCH GmbH. This is an open access article under the terms of the Creative Commons Attribution License, which permits use, distribution and reproduction in any medium, provided the original work is properly cited.

DOI: 10.1002/smssc.202300339

A. Lemaire, V. Van Speybroeck
Center for Molecular Modeling (CMM)
Ghent University
Technologiepark-Zwijnaarde 46, 9052 Zwijnaarde, Belgium

F. Liu
Collège de France, Chimie du Solide et de l'Energie—UMR 8260 CNRS
75005 Paris, France

F. Liu
Réseau sur le Stockage Electrochimique de l'Energie (RS2E)—FR, CNRS
3459
Amiens, France

M. L. Pinto
CERENA—Centro de Recursos Naturais e Ambiente, Departamento de Engenharia Química, Instituto Superior Técnico
Universidade de Lisboa
Av. Rovisco Pais, 1, 1049-001 Lisboa, Portugal

R. Demir-Cakan
Department of Chemical Engineering
Gebze Technical University
41400 Kocaeli, Turkey

and the existing interlayers are often composed of porous or dense conductive carbons.^[14,15] Nonetheless, due to the weak adsorption between nonpolar carbon-based materials and polar lithium polysulfides (LPS), the shuttle effect cannot be effectively suppressed.

Metal–organic frameworks (MOFs) are one of the latest classes of ordered micro- or mesoporous hybrid materials with highly tunable structural and/or chemical characteristics suitable for a wide range of applications from gas sorption, separation, catalysis, sensing to biomedicine, among others.^[16–19] This makes them highly promising candidates to limit polysulfides migration due to their unique structural and chemical properties, such as high porosity, uniform and tunable pore size, Lewis/Bronsted acidity, and structural defects, which shall significantly impact their molecular sieving ability.^[20–23] MOFs are expected here to play different roles: 1) as an ion sieving medium to allow selectively lithium ions to pass through while 2) preventing polysulfide ions from shuttling. Nonetheless, there is no consensus on what are the ideal parameters, e.g., particle size^[24,25] or structural features,^[12,26,27] to fulfill this role while clear-cut mechanistic studies are still lacking. Zirconium-based MOFs are a subset class of robust MOFs with a rare combination of chemical/thermal stability and highly versatile chemical/structural tunability; among a series of benchmark structures, the prototypical Zr terephthalate UiO-66 has been studied for Li–S batteries due to its micropores of 8–11 Å, the presence of structural defects which yield polar sites, and the possibility of incorporate polar functional groups in the linker. The combination of these features was shown to enhance polysulfides confinement.^[11,28,29] However, even with the structural defects and the introduction of functional groups, the length of the linker (terephthalate) limits the tuning of smaller pore sizes, requiring the development of stable materials with smaller pore size and higher density of active sites.

The benchmark Zr fumarate MOF-801(Zr) has been considered here as an alternative candidate owing to its narrow pores and its “polar” character, due to the high content of structural defects and the presence of numerous terminal –OH groups in the Zr oxo-cluster. Its three-dimensional cubic rigid structure, resulting from the assembly of $Zr_6O_4(OH)_4(CO_2)_{12}$ secondary building units and fumarate linkers, exhibit indeed smaller micropores (about 5–7 Å) than UiO-66 while possessing a large number of ligand defects particularly when a green low-pressure synthesis protocol is followed.^[30–32] This results in a large surface area of microporous material with a highly polar character, due to the presence of highly reactive acidic Zr–OH groups from the Zr_6 oxo-clusters. Structural defects are also expected to be beneficial to further limit the polysulfides migration.^[32,33] Moreover, Zr- and Ce-based MOFs have already been reported as catalytically active for the conversion of long-chains polysulfides in short-chains species, which enhances the electrochemical performance of the Li–S cells.^[34,35] Nonetheless, the use of the sole pristine MOFs as an interlayer presents several limitations: on one hand, the nonconductive nature of most MOFs limits the electron percolation and reactivation of the sieved polysulfides, associated with a poor Li-ion migration kinetics; on the other hand, pure MOF membranes present poor mechanical properties and often numerous defects. To circumvent the mechanical properties limitation, a mixed-matrix membrane (MMM) approach is a sound

approach. These composite membranes consist of an organic polymer matrix phase and an inorganic or hybrid solid filler phase, combining the required characteristics of these different materials and yielding materials with tailored permeability and selectivity.^[36] However, developing flexible interlayers that can effectively mitigate polysulfides and facilitate Li^+ transport to achieve high battery performance is still an ongoing challenge.

Recently a MOF-801(Zr)-carbon cloth composite has been proposed as interlayer for Li–S devices.^[37] The MOF-801 particles were directly grown into the carbon cloth support through an in situ solution crystallization method. Nonetheless, although one can observe the mitigation of the polysulfides shuttling to a certain extent, the mechanical stability of the MOF film at the surface of the carbon fibers was not discussed by the authors. Moreover, the host–guest interaction between the LPS was poorly addressed. In our case, we have designed a flexible free-standing MOF-based interlayer with high mechanical and chemical stability through a MMMs approach. This strategy allows to combine the chemical features of the three components of the composite: a) MOF-801, a robust microporous Zr-based MOF with a large pore volume and abundantly exposed Zr–OH active sites expected to enhance the polysulfides anchoring while facilitating Li^+ ions transport; b) Ketjen black (KB) carbon, a highly conductive carbon to enhance the electrical conductivity and improve the reactivation of sulfur species hosted in the MOF’s pores, while participating to the adsorption process due to its high surface area (around $1200\text{ m}^2\text{ g}^{-1}$); c) Poly(vinylidene fluoride-co-hexafluoropropylene) (PVDF-HFP), a polymer commonly used in battery field, known for its great mechanical properties and for allowing high filler loadings. The composite membranes were optimized in terms of porosity and mechanical properties and in-depth characterized through a combination of structural and morphological techniques, to understand the synergy between all components of the membrane, as well as solid-state nuclear magnetic resonance (NMR) and molecular dynamics (MD) to shed light on the polysulfides adsorption mechanism. Finally, the electrochemical behavior of Li–S cells containing MOF-801(Zr)/C/PVDF interlayer was studied and a significant improvement of the specific capacity (880 mA h g^{-1} after 50 cycles) was found when compared to the cells containing only the routine glass fiber separator.

2. Results and Discussion

2.1. Synthesis and Polysulfides Adsorption Test of MOF-801(Zr)

MOF-801(Zr) nanoparticles were prepared through a room-temperature synthesis method already reported by us.^[32] The powder X-ray diffraction (PXRD) pattern (Figure S1a, Supporting Information) of the obtained MOF-801(Zr) was found to be in good agreement with the simulated one, confirming the purity and crystallinity of the obtained compound. The transmission electron microscopy (TEM) (Figure 1a) and scanning electron microscopy (SEM) (Figure S1b, Supporting Information) images showed that MOF-801(Zr) nanoparticles exhibit a spherical crystal morphology with a particle size dispersion comprised between 40 and 80 nm, in agreement with the literature.

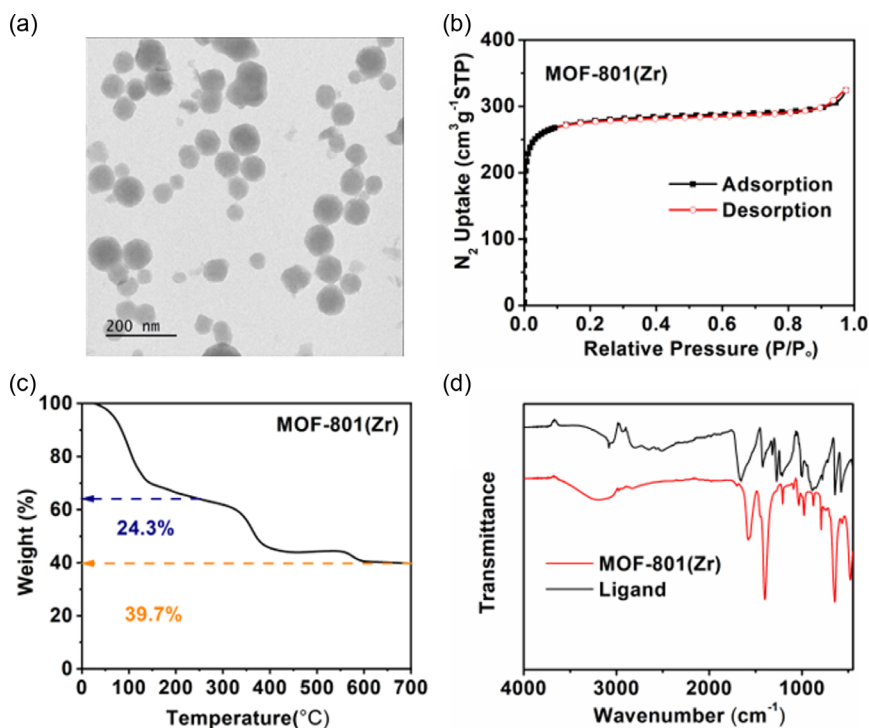


Figure 1. a) TEM images of MOF-801 (Zr) nanoparticles; b) N_2 adsorption–desorption isotherms at 77 K ($P_0 = 1$ atm) of MOF-801 (Zr); c) TGA of MOF-801 (Zr) under oxygen atmosphere (heating rate of $3\text{ }^\circ\text{C min}^{-1}$); and d) Fourier-transform infrared spectroscopy (FT-IR) spectra of MOF-801 (Zr) and fumaric acid (ligand).

To investigate the microstructure of MOF-801(Zr), N_2 adsorption–desorption analysis (Figure 1b) was performed at 77 K, resulting in a high specific surface area of $1020(\pm 20)\text{ m}^2\text{ g}^{-1}$, calculated through the Brunauer–Emmett–Teller (BET) method. In addition, the pore size distribution (PSD) (Figure S1c, Supporting Information) calculated by the nonlocal density functional theory (NLDFT) ($-N_2$ method, revealed the microporosity (5–13 Å) of the synthesized MOF-801. The expanded PSD correlated further confirming the defective nature of MOF-801(Zr). Hence, these results have demonstrated the suitability of MOF-801(Zr) as an ideal molecular sieve for blocking large-sized Li_2S_8 ($\approx 2\text{ nm}$ length)^[14] while letting the lithium ions (ionic diameters: 0.12 nm) pass.^[31] Based on the residual content of ZrO_2 obtained from thermogravimetric analysis (TGA), the ligand connectivity of the Zr_6 oxocluster was calculated to be 7.94, which contrasted with the theoretical connectivity of 12 for the defect-free structure. This calculation supported the presence of a significant number of missing ligands within the solid. Additionally, following recent systematic studies on MOF defect quantification,^[32,38] we decomposed the MOF in an alkaline medium and conducted ^1H NMR analysis. As shown in Figure S1d (Supporting Information), a substantial amount of formate was observed, with a formate: fumarate molar ratio of 1:4.73, indicating a significant replacement of the fumarate linker by formate. Combining these results with the N_2 adsorption data ($1200\text{ m}^2\text{ g}^{-1}$ in this case compared to $650\text{ m}^2\text{ g}^{-1}$ for defect-free MOF-801), we could conclude that the synthesized MOF-801 possessed a large number of defects. The FT-IR spectra showed a large number of vibrations of $-\text{OH}$ groups and strong vibrations

associated to COO^- groups coordinated to Zr^{IV} , while almost no trace of uncoordinated fumaric acid ($\approx 1644\text{ cm}^{-1}$) was observed, which further indicated that the as-prepared pure MOF-801(Zr) possess a large number of terminal or bridging $\text{Zr-OH}/\text{H}_2\text{O}$ polar groups suitable to interact strongly with polysulfides of various lengths.

To investigate the capability of MOF-801(Zr) to efficiently adsorb polysulfides, 50 mg of MOF-801(Zr) was added into 1 mL of 0.05 M Li_2S_6 solution. Within 30 min, the solution became colorless. The MOF powder, initially white, turned yellowish in polysulfide-containing solution, suggesting the strong interaction of the Zr-oxoclusters with polysulfides (Figure 2a). After self-standing for one week, the structural integrity of MOF-801 exposure to polysulfides was confirmed by PXRD (Figure 2b). Characteristic reflections of elemental sulfur could be observed, nonetheless, this was certainly ascribed to the crystallization of sulfur during the sample drying, as for the wet sample no sulfur peaks were observed (Figure S1e, Supporting Information). Different concentrations of polysulfides were in parallel tested to determine the detection limit of the dissolved polysulfides by UV–vis spectroscopy (Figure 2c).

To better discriminate the solutions with different polysulfide concentrations, the first derivatives of the UV–vis spectra were compared.^[39,40] For each concentration, typical peaks in the UV–vis spectra derivative could be observed, with a peak shift to the UV region as the concentration decreases. As shown in Figure 2d, the concentration of 0.05 M Li_2S_6 solution decreased to $5 \times 10^{-4}\text{ M}$ after adding MOF-801 for 24 h, which further quantitatively demonstrates the ability of MOF-801(Zr) to adsorb

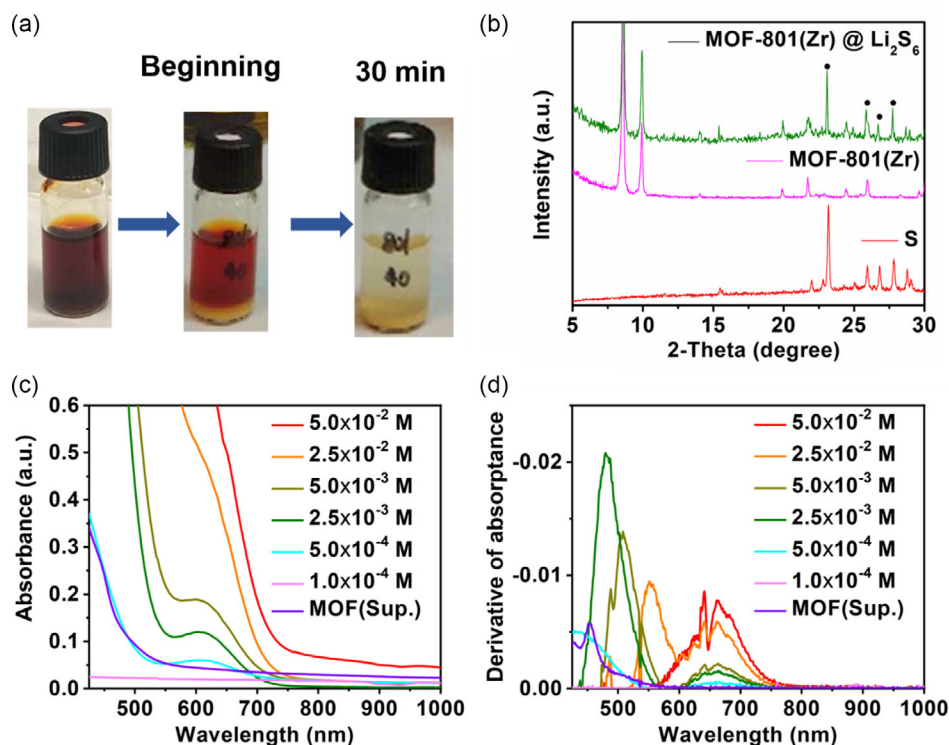


Figure 2. a) Polysulfides adsorption test; b) PXRD pattern of powder samples before and after polysulfide adsorption test ($\lambda_{Cu} \approx 1.5406 \text{ \AA}$); c) UV-vis absorption spectra of Li₂S₆ at different concentrations solutions and 0.05 M Li₂S₆ solution after adding MOF-801 for 24 h which named MOF(Sup.); and d) first derivatives of the UV-vis spectra.

polysulfides. This could be ascribed to the microporous structure nature of MOF-801 and the presence of abundant polar sites within the pores.^[7,41] The adsorption properties of MOF-801 after incorporation in a PVDF-HFP matrix have also been tested (Figure S2, Supporting Information). When compared with the base PVDF-HFP membrane, the MOF-based membrane effectively limits the diffusion of the polysulfide species.

2.2. Solid-State NMR

Although numerous studies about polysulfides selective adsorption with MOF-based modified separators or interlayers can be found in the literature, very few reported the study on the host-guest interactions. To shed light on this phenomenon, magic-angle spinning (MAS) solid-state NMR experiments were performed on ¹H, ⁷Li, and ¹³C.

As shown in Figure 3a, the peak widths of fumarate (¹³C: ≈ 172 ppm for carbonate, ≈ 138 ppm for double bond; ¹H: ≈ 7.0 ppm for double bond) and formate (¹³C: ≈ 168 ppm; ¹H: ≈ 8.0 ppm) became broader upon Li₂S₆ absorption. Note that the traces of formate groups were still found (see Figure S3 for assignment, Supporting Information)^[42] originating from the formic acid used during the MOF synthesis and not completely removed during the washing process. In the Li₂S₆-loaded MOF-801(Zr), a new ¹³C site of around 175 ppm emerged and it can be attributed to the thermal decomposition of dioxolane solvent during the preparation of the polysulfides solution since only a correlation between the new ¹³C site and the proton from solvent

was observed. The observed NMR line-broadening effect implies that the MOF-801(Zr) has experienced a change in the chemical environment due to the loading of Li₂S₆ within the pores. The interaction between Li and the MOF-801 framework was also confirmed by the 1D ⁷Li spectrum and the 2D ⁷Li-¹H correlation experiment (Figure S4, Supporting Information), where the adsorbed ⁷Li and the cross peaks between lithium and fumarate are observed. To locate lithium in MOF-801(Zr), ⁷Li-¹³C REDOR experiments were performed to determine the distances between lithium and various carbon sites. As shown in Figure 3b, the nearest lithium is $3.3 \pm 0.5 \text{ \AA}$ to the carbon of carboxylate (⁻¹³COO) in fumarate. Following that, it can be estimated that the distance between the ⁷Li and the double bond ¹³C signal (¹³C=¹³C) is between 3.3 and 5.0 \AA (Figure 3c). The measurement is less precise in the latter case due to the low sensitivity resulted from the line-broadening effect. More accurate distances are expected to be obtained by using ¹³C-labelled fumaric acid for the synthesis of the MOF.

Hence, the results suggest that the lithium atoms are located within the overlapped zone bounded by the two shells in Figure 3b,c. This indicates that lithium is rather closer to Zr₆ oxoclusters, and, hence, closely interacting with the carboxylate group. Moreover, the ¹³C centerband-only detection of exchange (CODEX) result (Figure S5, Supporting Information) suggests that there are two lithium staying close to each other, i.e., there is only a single (not a cluster) lithium polysulfide chain in the vicinity. Nonetheless, due to the lack of reliable measurements on reference samples, the exact distance between the two lithium

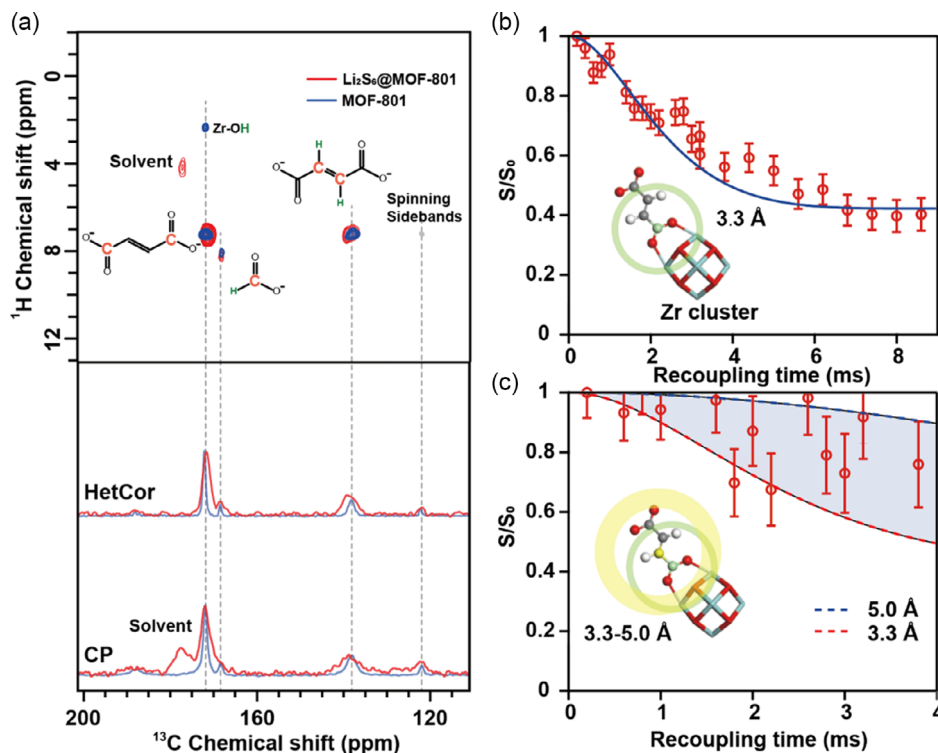


Figure 3. Solid-state NMR results. a) ^1H - ^{13}C HETCOR spectra (top) of pristine MOF-801 (Zr) (blue) and Li_2S_6 -loaded MOF-801 (red), and projection of 2D HETCOR spectra to the ^{13}C dimension (middle) and ^1H - ^{13}C CP spectra (bottom). ^7Li - ^{13}C REDOR dephasing curves due to the coupling of lithium and carboxyl carbon (≈ 3.3 Å); b) or the coupling of lithium and double bond carbon (≈ 3.3 – 5 Å); c) of fumarate in Li_2S_6 -loaded MOF-801. The possible lithium positions are highlighted by the faint yellow and green shells and the yellow atom refers to the carboxylate carbon atom.

atoms could not be determined, which could have helped to identify the shape of the chain.

2.3. MD Simulations

Additional insight into the host–guest interactions between MOF-801 and Li_2S_6 could be obtained from MD simulations. The MOF-801 model structure used in the simulations has Zr_6 oxoclusters with an eightfold linker connectivity, in agreement with the experimental measurements where a ligand-to-metal ratio close to 8 was deduced. The most straightforward approach to simulate an eightfold linker connectivity consists of removing one Zr_6 oxocluster along with the 12 attached linkers

from the pristine MOF-801 unit cell. This merges the tetrahedral pores of MOF-801 into a larger pore with a diameter of about 13.5 Å (Figure S6, Supporting Information). The remaining metal nodes in the unit cell are terminated with formate.

To probe both the host–guest and guest–guest interactions for MOF-801 and Li_2S_6 , different Li_2S_6 loadings were considered (ranging from 4 to 10 Li_2S_6 molecules per unit cell). The dominant interactions could be identified by calculating radial distribution functions (RDFs) for different atom pairs. The lithium atoms were shown to interact primarily with the oxygen atoms of the fumarate linkers and the formate groups grafted to the Zr_6 oxocluster, resulting in an RDF peak at about 2 Å (Figure 4a), which confirmed the host–guest interactions also

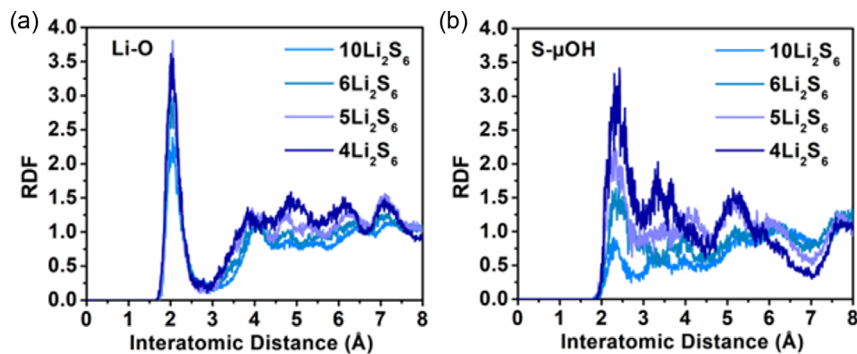


Figure 4. RDFs for a) Li–O and b) S– H_{OH} atom pairs obtained from first-principles MD simulations of MOF-801 with different Li_2S_6 loadings.

observed in the NMR experiments. For sulfur, the interaction with the μ -OH groups on the metal nodes was most pronounced, resulting in an RDF peak at about 2.3 Å (Figure 4b). When different Li_2S_6 molecules are in close proximity during the MD simulation, they also showed a strong tendency to interact with one another to form a larger polysulfide cluster.

Also for a second MOF-801 model with a ninefold linker connectivity, which is obtained by only removing linkers from the pristine structure, similar conclusions could be drawn. As the metal nodes in this second model are terminated with OH-groups and a water molecule instead of with formate, the Li-O RDF peak at about 2 Å now contains contributions from the oxygen atoms of both the fumarate linkers and the $-\text{OH}/\text{H}_2\text{O}$ terminations of the metal nodes (Figure S7, Supporting Information). Similarly, the sulfur atoms can now interact with the μ -OH groups on the metal nodes as well as the additional $-\text{OH}/\text{H}_2\text{O}$ terminations (Figure S7, Supporting Information).

This new approach, based on a combination of experimental data from solid-state NMR and MD simulation, allowed to unravel for the first time the preferential interaction of the polysulfides with the host MOF structure. The lithium atoms preferentially interact with the carboxylate groups, as sustained by the ^7Li - ^{13}C coupling observed by solid-state NMR and by the Li-O peak in the RDF. The S- μ -OH interaction from RDF also sustains a close interaction of the polysulfides with the Zr6 oxocluster, through the terminal acidic Zr-OH groups.

2.4. Preparation of MOFs-Based MMM Interlayers

To investigate the efficiency of MOF-801(Zr) in Li-S devices, a functional free-standing interlayer material was prepared through a MMM approach. MOF-801(Zr)-based composite membranes with good flexibility and enhanced electrical conductivity were designed, to overcome the mechanical brittleness and insulator character of the pristine MOF.^[43] To reach that goal, a three-component composite was investigated, combining MOF-801 nanoparticles for the sieving and shuttle effect mitigation, KB particles for the conductivity, and a polymer for the mechanical processability (Table S2, Supporting Information).

MOF-801-based MMMs with flat surfaces were first prepared through a blade casting method and recovered as mechanically stable self-standing films (Figure S8a, Supporting Information). Flexible polymers are known to easily wrap MOF nanoparticles, provided that their respective charge surface displays opposite values, which enhances the attraction between both moieties. Such parameter is crucial for obtaining defect-free membranes since the particles should be homogeneously distributed within the membrane without agglomerate. As demonstrated for PVDF or poly (ethylene oxide) (PEO) and UiO-66, the end groups of polymers can penetrate to some extent into the pores of the MOF, depending on the chemical affinity between the polymer chains and the MOF.^[44] The main possible drawback is pore blocking, leading in some cases to a strong decrease of accessible porosity.^[45] To confirm the interactions between PVDF-HFP and MOF-801(Zr) nanoparticles, N_2 porosimetry analysis of MOF-801(Zr) MMMs was performed. For 30 wt% MOF-801(Zr) 70 wt% PVDF-HFP MMMs, if the MOF's pore is not blocked at all, the BET-specific surface area should be around

$300 \text{ m}^2 \text{ g}^{-1}$, nonetheless, the experimental value is only $167(\pm 1) \text{ m}^2 \text{ g}^{-1}$ (Figure S8b, Supporting Information), indicating that some polymer chains enter the pores of the MOF and partially block access to the N_2 molecules at 77 K, in agreement with what was already observed for UiO-66/PVDF system.^[44] Note that the MOF-801(Zr) after the introduction in the membrane retains its crystalline structure (Figure S9, Supporting Information). As the polymer chains partially enter into the pores, further reducing the pore size, this is a priori a favorable parameter to physically block polysulfides, while still enabling a fast Li^+ (ionic diameters: 0.12 nm) conduction.^[46]

To prepare conducting membranes, KB was also added to the composite. To determine the optimal ratio of MOF and KB in the membrane, samples containing 10, 20, and 30 wt% KB were prepared (Figure 5 and S10–S12, Supporting Information), and their electrochemical behavior was characterized by galvanostatic cycling tests. Figure S12 (Supporting Information) shows that the cell with the interlayer with 30 wt% KB and 30% MOF-801(Zr)/PVDF-HFP MMM exhibits the highest specific capacity and stability. Thus, the optimized MMM of 30 wt% KB was adopted in the following studies, named MOF-801(Zr)/C/PVDF-HFP MMM, hereafter. Noteworthy, the flexible MOF-801(Zr)/C/PVDF-HFP MMM can be curled at will and has excellent mechanical properties (Figure 5b). The SEM images showed that the membrane is flat with a thickness of 15.6 μm (Figure 5c). Inside the membrane (Figure S13, Supporting Information), MOF nanocrystals and KB nanoparticles look tightly packed and the voids between the particles are filled up with PVDF-HFP polymer, forming a quite dense composite. The SEM elemental mapping (Figure 5d) showed uniform distributions of F and Zr in MMM, demonstrating that PVDF-HFP and MOF-801(Zr) form a fairly even distribution.

Visualization of the internal structure of MMMs is of great interest in materials science to get a better understanding of the membrane's mechanical stability and its properties.^[47–49] In this context, 3D X-ray microscopy is a powerful tool that allows for high-resolution imaging of the internal structure of MMMs. As shown in Figure 5e, 3D X-ray microscopy images revealed a uniform distribution of MOF-801(Zr) and carbon particles within the polymer matrix. Despite the presence of a limited number of particle aggregates (Figure 5f), the overall distribution looks on the whole homogeneous, indicating a well-dispersed particle configuration. Furthermore, the quantitative analysis of the membrane revealed a MOF-801(Zr) content of approximately 28 vol%, in good agreement with the initial content of 30 wt% added during the membrane preparation, considering that the MOF particles are denser than the KB and PVDF-HFP polymer. This confirms the robustness of the fabrication process used in this study, and that MMM with a homogeneous particle distribution could easily be prepared.

To evaluate the effectiveness of the composite interlayer in the “shuttle effect” mitigation, the electrochemical behavior of Li-S cells was finally evaluated. The self-sustained composite membrane was placed between the cathode and the routine glass fiber separator and cycled against lithium metal. Figure 6a shows the galvanostatic charge–discharge cyclic behavior of the batteries at 0.1 C.

The batteries with MOF-801(Zr)/C/PVDF-HFP MMM interlayer exhibited an initial capacity of 1110 mA h g^{-1} , while a high

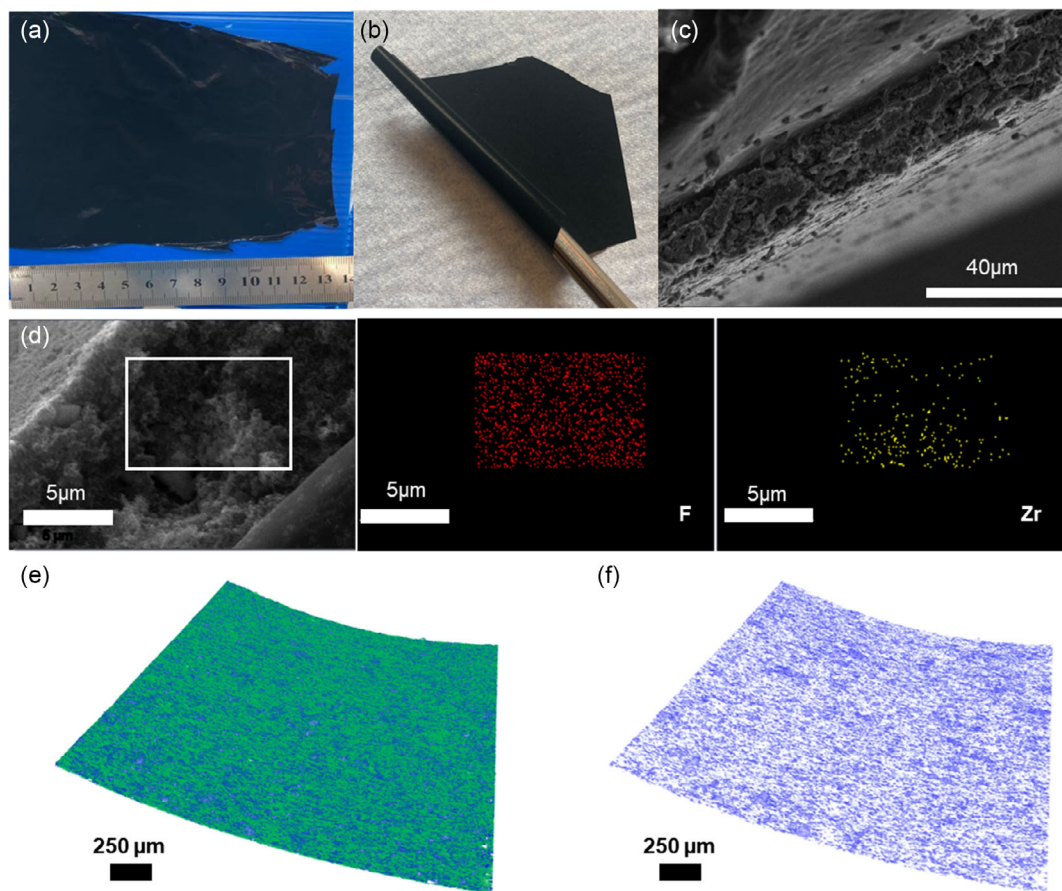


Figure 5. a,b) Photographs of the MOF-801(Zr)/C/PVDF-HFP MMM (30 wt% KB); c) cross-sectional SEM image of the MOF-801(Zr)/C/PVDF-HFP MMM; d) cross-sectional SEM image of the MOF-801(Zr)/C/PVDF MMM and the corresponding elemental mapping images of F and Zr. e,f) 3D X-ray microscopy images of the composite membrane MOF-801(Zr)/C/PVDF MMM (30 wt% KB) with the mapping of the MOF-801(Zr) particles spatial distribution within the composite membrane in blue.

discharge capacity of 880 mA h g^{-1} was still retained after 50 cycles. The reproducibility of these results over 3 cells is shown in Figure S14 (Supporting Information). For comparison, the blank, the PVDF-HFP, and the MOF-801(Zr)/PVDF-HFP MMM delivered 647, 511, and 620 mA h g^{-1} , respectively, over 50 cycles. The higher capacity retention indicates that the MOF-801(Zr)/C/PVDF-HFP MMM interlayer was able to effectively improve the cycling performance of Li-S batteries. The FT-IR spectrum of the MOF-801(Zr)/C/PVDF-HFP MMM interlayer after 50 cycles did not show any ligand's peak, confirming the stability of MOF-801(Zr) particles after cycling (Figure S15, Supporting Information). Furthermore, although it is hard to establish a direct comparison between this work and the ones found in the literature for UiO-66(Zr) based membranes^[11,28] one can note that for the MOF-801(C)/PVDF-HFP membrane after 50 cycles the capacity retention (880 mA h g^{-1}) is higher than the one observed for a pristine UiO-66 layer deposited in a polypropylene separator (720 mA h g^{-1} at 0.5 C after 500 cycles) and slightly lower than a UiO-66/super P based functional separator (964 mA h g^{-1} at 0.5 C after 200 cycles). These discrepancies can be attributed to several factors: 1) not the same membrane architecture - no interlayers but functional

separators; 2) different cycling rates (0.5 C vs 0.1 C in this work); 3) the content and the type of conductive carbon, and 4) the different structural features of these two frameworks (not the same linker, defects ratio).

In Figure 6b, two oxidation peaks and two reduction peaks could be observed in the cyclic voltammetry (CV) curves of Li-S batteries with MOF-801(Zr)/C/PVDF-HFP MMM interlayer. The reduction peaks at about 2.28 and 1.98 V correspond to the reduction of S_8 to Li_2S_n ($4 \leq n \leq 8$) and Li_2S_n ($4 \leq n \leq 8$) to $\text{Li}_2\text{S}/\text{Li}_2\text{S}_2$, respectively.^[50] In addition, the peaks of the cell with the MOF-801(Zr)/C/PVDF-HFP MMM interlayer were shown to be sharper, and the peak currents were larger than the batteries without the interlayer, demonstrating that the MOF-801(Zr)/C/PVDF-HFP MMM interlayer improves the electrochemical kinetics of Li_2S_n conversion. The kinetic improvement by this MMM was also confirmed by the electrochemical impedance spectroscopy (EIS) results. The EIS Nyquist plots of batteries with equivalent circuits are shown in Figure 6c, R1 reflects the contact resistance between the electrode and the electrolyte, R₂ reflects the resistance of charges transfer at the interface of the cathode, and R₃ reflects interfacial layer resistance at the surface of the anode. The best charge-transfer capability of this optimized

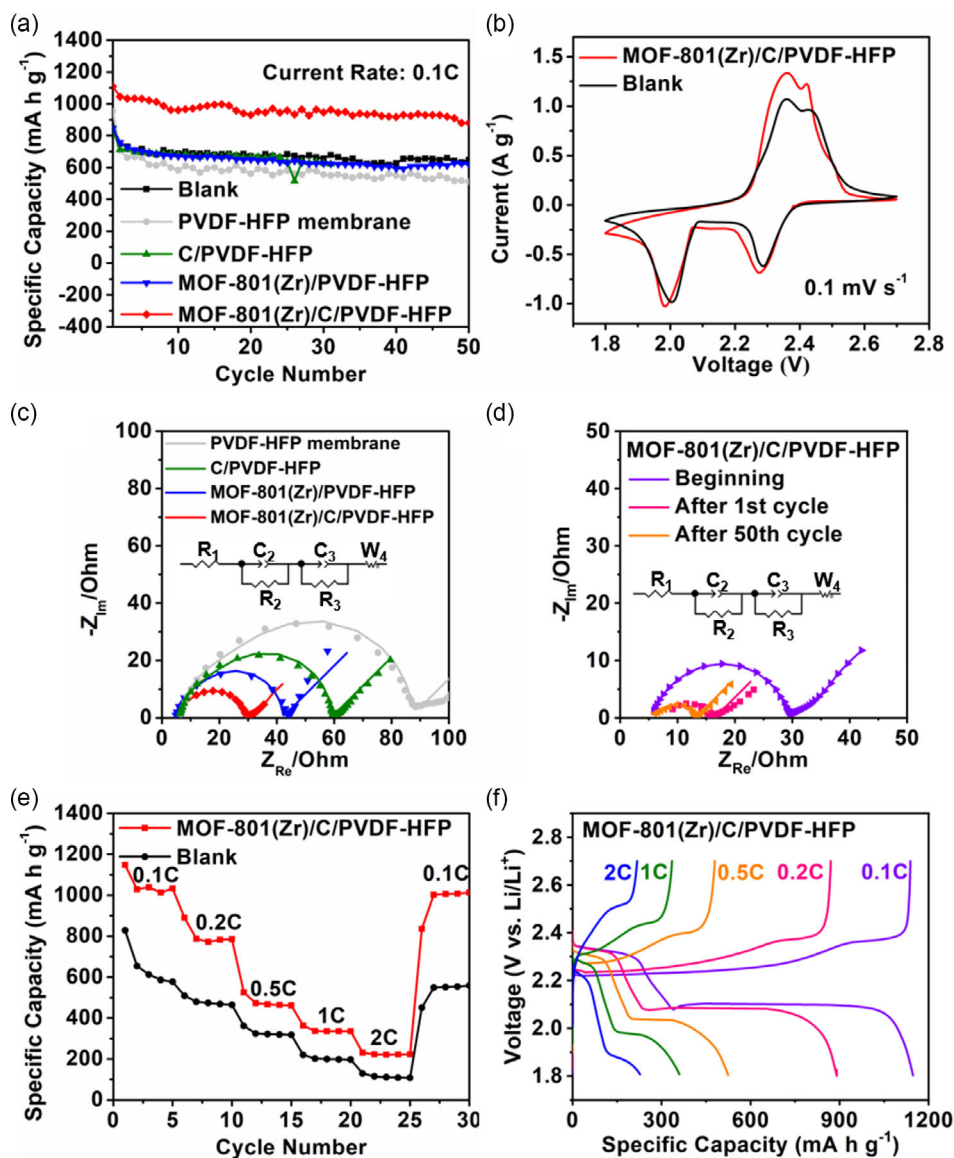


Figure 6. a) Galvanostatic cycling performance at 0.1 C; b) the CV profile of Li-S batteries with and without the MOF-801(Zr)/C/PVDF-HFP MMM interlayer at 0.1 mV s⁻¹; c) EIS profiles (dots are raw data, lines are fitted data). d) EIS profiles; e) galvanostatic cycling performance of batteries with the MOF-801(Zr)/C/PVDF-HFP MMM interlayer and without interlayer (blank) at different current densities; and f) galvanostatic charge-discharge curves at different current densities.

interlayer was evidenced by the lowest R_2 value (6.827 Ω) than that of the other membranes: MOF-801(Zr)/PVDF-HFP MMM (6.863 Ω), C/PVDF-HFP MMM (11.01 Ω), and PVDF-HFP membrane (18.07 Ω) (Table S3, Supporting Information). Such a low value can tentatively be explained by the abundant exposed O active sites and Zr-OH sites on Zr6 oxo-cluster limiting polysulfides and promoting the sulfur redox reaction kinetics, as sustained by solid-state NMR and MD calculation results. Furthermore, as shown in Figure 6d and Table S4 (Supporting Information), the impedance value of the MOF-801(Zr)/C/PVDF-HFP MMM cell showed similar values between 1st cycle (4.326 Ω) and 50th cycle (4.248 Ω), evidencing its stability upon cycling. This can be attributed to the interlayer effectively

limiting the diffusion of polysulfides. Figure 6e shows the rate performance of the cell with MOF-801(Zr)/C/PVDF-HFP MMM interlayer and Figure 6f the corresponding galvanostatic charge-discharge profiles at different current densities, where the enhancement of the cycling performance at low rates can be clearly seen when using the MOF-based composite membrane. At higher rates, the improvement related to the blank cell is more limited, certainly due to the kinetics of the complex redox reaction of sulfur. Finally, when the current was switched back to 0.1 C, the cell could be recovered and maintained at 1013 mA h g⁻¹ at the 30th cycle, indicating its excellent rate capability. The percentage retention is represented in Figure S16 (Supporting Information).

As mentioned above, the chain of the PVDF-HFP polymer partially enters into the micropores of the MOF-801(Zr), leading to a slight pore size narrowing. To evaluate if this would impact the Li⁺ diffusion within the membrane symmetric cells containing the MMM were assembled. The MOF-801(Zr)/C/PVDF-HFP MMM was paired between two stainless steel (SS) plates to make an SS | MMM | glass fiber (GF) | SS cell with electrolyte (1 M LiTFSI and 0.25 M LiNO₃). The value of ionic conductivity can be calculated from EIS according to the following equation:

$$\sigma = d/(RA) \quad (1)$$

σ is the ionic conductivity (S cm⁻¹), d is the thickness of the separator (cm), R is the resistance (Ω), and A is the area of the stainless-steel electrode (cm²).^[51,52] As shown in Figure S17 (Supporting Information), the EIS of the GF separator illustrates a larger resistance (10.44 Ω), while the optimized MMM interlayer with the GF separator shows a resistance of 4.04 Ω . The calculated Li⁺ conductivity for this interlayer with the GF separator was 19.03 mS cm⁻¹, which is higher than that of the GF separator (7.22 mS cm⁻¹), indicating that the Li⁺ percolates faster when the MOF-801(Zr)/C/PVDF-HFP MMM interlayer was added than when only GF separator is used. Compared with the macropores in the original GF separator which allow solvated Li⁺ to pass through, the sub-nanopores in the MOF/C-based MMM are smaller than the diameters of solvated Li⁺. This is likely to cause the desolvation of Li⁺ when diffusing through

the sub-nanochannels under an electric field, which might facilitate subsequent fast Li⁺ conduction.^[46,53,54]

To further evaluate the charge-transport characteristics, CV measurements under different scan rates from 0.2 to 0.5 mV s⁻¹ (Figure 7) were conducted. A distinguishable peak shift could be observed with the increase of the scan rate, leading to an increase of the polarization voltage at higher rates. It is clear that the cell with our hybrid interlayer showed a smaller peak shift with increasing scanning rate for O1 peaks (60 mV), R1 peaks (30 mV), and R2 peaks (60 mV) than without interlayer for O1 peaks (62 mV), R1 peaks (32 mV) and R2 peaks (61 mV), suggesting improved kinetics for Li⁺ transport and lithiation/delithiation process.^[55,56] Lithium-ion diffusion coefficient D_{Li^+} (cm² s⁻¹) was calculated according to the Randles-Sevcik equation:

$$I_p = (2.687 \times 10^5) n^{3/2} A C_{Li^+} (D_{Li^+} \nu)^{1/2} \quad (2)$$

in which I_p (in A) is the peak current, n represents the number of electrons in the reaction (for Li-S batteries, $n = 2$), A (in cm²) indicates the electrode area (1.327 cm²), C_{Li^+} (mol mL⁻¹) means the lithium-ion concentration, and ν stands for the scanning rate (V s⁻¹).^[57-59] As shown in Table 1, the values of D_{Li^+} for the cell with the MMM interlayer at all three peaks in CV curves show higher D_{Li^+} when compared with those of blank cell, further demonstrating the faster Li⁺ diffusion rate and reaction kinetics. This may be due to the existence of abundant polar

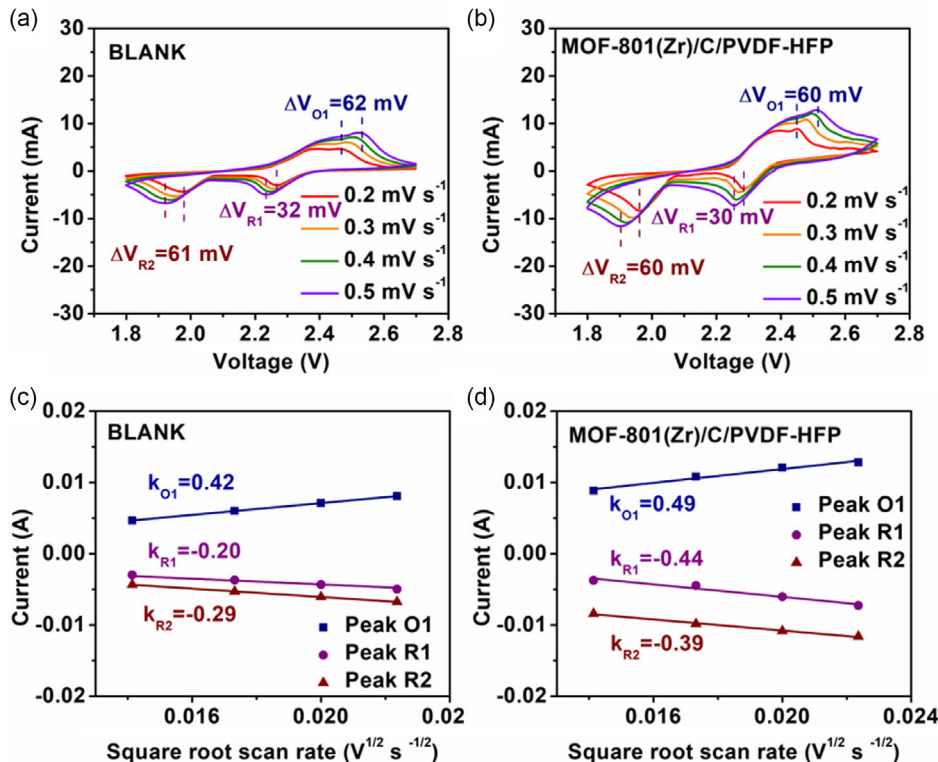


Figure 7. a) CV plots of Li-S batteries; b) CV plots of Li-S batteries with MOF-801(Zr)/C/PVDF-HFP MMM interlayer at different scan rates; c) corresponding linear fits of the peak current of CV plots of blank cell; and d) corresponding linear fits of the peak current of CV plots of cell with MOF-801(Zr)/C/PVDF-HFP MMM interlayer.

Table 1. The Li⁺ diffusion coefficient.

Li ⁺ diffusion coefficient [1 × 10 ⁻⁸ cm ² s ⁻¹]	Blank	MOF-801(Zr)/C/ PVDF-HFP MMM
Peak O1	11.10	15.11
Peak R1	2.52	12.18
Peak R2	5.29	9.57

groups such as –OH on MOFs, which are beneficial to the reaction kinetics of Li⁺.^[11]

3. Conclusion

We have designed a new type of freestanding microporous zirconium MOFs-based MMM interlayer based on nanoparticles of the Zr fumarate MOF-801, a KB porous carbon, and PVDF-HFP. We could first demonstrate through a combination of experimental data from solid-state NMR and MD calculations that the host–guest interaction between the polysulfides and the MOF structure relies not only in the polar nature of the acidic Zr-OH terminal groups but also in the polar character of the carboxylate moieties of the fumarate linker. Incorporating MOF-801(Zr) and KB into a PVDF-HFP matrix led to a hybrid interlayer in Li–S batteries, with a remarkable improvement in the initial capacity up to 1110 mA h g⁻¹, which was retained at a significant 880 mA h g⁻¹ after 50 cycles. Electrochemical advanced characterizations demonstrated that the MOF-based interlayer facilitates the diffusion of Li⁺ while effectively anchoring polysulfides and promoting their redox conversion, thus explaining the enhanced performance of the Li–S batteries. The development of MOF-801(Zr)-based MMM interlayers not only represents a promising approach for improving the performance of lithium–sulfur (Li–S) batteries, but these findings pave the way for a general strategy to prepare advanced MOF MMMs with enhanced electrochemical properties. By considering different MOF compositions and fillers, one could design a series of customized multifunctional interlayers with superior performance in Li–S batteries according to specific requirements in energy storage applications and beyond.

4. Experimental Section

Preparation of MOF-801(Zr) Nanoparticles: Synthesis of nanoparticles of MOF-801(Zr): 10.86 mmol of ZrOCl₂·8H₂O, 7.624 mmol of fumaric acid, 9 mL of formic acid, and 40 mL of deionized water were added in the reactor.^[32] The solution became cloudy within 5 h, indicating the formation of MOF-801(Zr) nanoparticles. The product was collected by centrifugation, and washed with water and ethanol. The prepared MOF-801 was finally dried at room temperature 100 °C under the vacuum overnight before use.

Preparation of MMMs: MOF-801(Zr), KB carbon, and acetone were added to a glass vial and then sonicated to obtain a uniform suspension. After that, 5% PVDF-HFP in acetone solution was added to the MOF suspension. After stirring, the homogeneous MOF-801(Zr)/C/PVDF-HFP slurry was cast onto a glass substrate with a micrometric film applicator (Elcometer 3570/1). The coated membranes were dried in the air. See Table S1 (Supporting Information) for detailed information.

Preparation of Sulfur Cathodes and Assembly of Li–S Cells: C/S composites were prepared by mixing acetylene carbon black and sulfur powder in

a mass ratio of 4:6. The mixture was heated to 160 °C at the rate of 1 °C min⁻¹, then cooled to room temperature. As prepared C/S composites and PTFE (10%w PTFE) with a mass ratio of 0.95: 0.05 were mixed in EtOH. After grinding, the uniform pastry was rolled on a flat surface until it became homogeneous, then punched to 1.327 cm², and finally vacuum dried at 80 °C overnight. The average sulfur loading for each cathode was ≈2.5 mg cm⁻².

The Li–S cells were assembled in an argon-filled glovebox. CR2032-type coin cells were used, with S/C composite as the cathode, the MOF-based interlayer directly placed after the cathode, the routine glass fiber separator, and finally lithium metal as the anode. The electrolyte was 1 M LiTFSI (lithium bis(trifluoromethanesulfonyl)imide) in 1,2-dimethoxyethane (DME) and 1,3-dioxolane (DOL) (1:1 v/v) with 0.25 M LiNO₃ as an additive. The amount of electrolyte added to each cell was 15 μL electrolyte per 1 mg sulfur.

Material Characterization: All chemicals were purchased from commercial suppliers and used as received without further purification. PXRD data were recorded on a high-throughput Bruker D8 Advance diffractometer working on transmission mode and equipped with a focusing Göbel mirror producing CuKα radiation (λ = 1.5418 Å) and a LynxEye detector. Nitrogen porosimetry data were collected on a Micromeritics Tristar instrument and Micromeritics Triflex adsorption analyzer at 77 K (preactivating at 373 K 12 h). SEM observations were performed using the FEI Magellan 400 scanning electron microscope. TEM images were recorded with a JEOL 2010 transmission electron microscope operating at 200 kV. TGA data were collected on Mettler Toledo TGA/DSC 2, STAR System apparatus with a 5 °C min⁻¹ heating rate under oxygen flow. The self-sustained films were cast using an Elcometer 3570/1 micrometric film applicator, which can be adjusted in 1 micron intervals, from 0 to 1 mm using a micrometric screw. A Büchi glass oven B-585 was used for drying and vacuum transfer. Ultraviolet spectroscopy measurements were performed in quartz cells and in a UV-1800 Shimadzu spectrometer.

Adsorption Tests of Li₂S₆: The 50 mM Li₂S₆ electrolyte was obtained by mixing 1 mmol of Li₂S and 5 mmol of S. 10 mL of DOL, and 10 mL of DME were added to the vial and the solution was heated under stirring at 70 °C for 24 h in an argon-filled glovebox. The 50 mg as-prepared MOF samples were added into 1 mL of 0.05 M Li₂S₆ solution to confirm polysulfides adsorption.

Solid-State NMR: The solid-state NMR spectra were acquired at an 18.8 T/800 MHz spectrometer equipped with a Bruker Avance Neo console. The cross-polarization (CP) contact time used in the ¹H-¹³C heteronuclear correlation (HETCOR) and ⁷Li-¹H CP-heteronuclear single-quantum coherence^[60] experiments are 2.5 ms and 200 μs, respectively. We have implemented frequency-switched Lee–Goldburg (FSLG) homonuclear ¹H decoupling during the ¹H evolution period to achieve narrower lines in HETCOR.^[61] Note that the ¹H chemical shift dimension is corrected by a numerical factor of cos(54.7°) due to FSLG. The CODEX^[62] experiments were performed on a 3.2 mm HXY MAS probe. The ⁷Li-¹³C rotational echo double resonance (REDOR) experiments were performed on a 2.5 mm HXY MAS probe. In the REDOR experiment,^[63] the ¹H-¹³C CP was first used to polarize ¹³C, followed by ¹³C-⁷Li recoupling π pulses applied on ⁷Li channel with ¹³C detection. The MAS spinning frequencies are 10 kHz in all experiments. The ¹H and ¹³C chemical shifts were referenced to the adamantane signal at 38.5 ppm.

MD Simulations: To probe the interactions between the MOF-801 host material and Li₂S₆ guest molecules, first-principles MD simulations were performed with the CP2K quantum chemistry software package.^[64] The molecular interactions were modeled with density functional theory (DFT) using the Perdew–Burke–Ernzerhof (PBE) functional^[65] with DFT-D3(BJ) dispersion corrections.^[66] All the simulations were performed in the (N, P, σ_a = 0, T) ensemble so that the shape of the unit cell is flexible. The temperature of the simulations was set to 300 K, while the pressure was set to 1 bar. The temperature and pressure were, respectively, controlled by a Nosé–Hoover thermostat^[67,68] with a time constant of 0.1 ps and an MTTK barostat^[69] with a time constant of 1 ps. The plane wave basis set used a cutoff of 800 Ry and was combined with the TZVP-MOLOPT basis set^[70] and Goedecker, Teter, and Hutter (GTH) pseudopotentials.^[71] Each MD simulation is at least 5 ps long.

3D X-Ray Microscopy: The composite membranes were scanned by nano-CT (SkyScan 2214, Bruker, Belgium) equipped with an X-ray tube using a W source (operated at 110 kV and 170 μ A) and a charge coupled device (CCD) detector. Images of the MOF-801(Zr)/C/PVDF-HFP MMM were obtained employing no filter and with a voxel resolution of 1.0 μ m. The capillaries were rotated 360° during data acquisition. Images were taken every 0.15°, i.e., 2401 frames, with an exposure time of 3700 ms. The geometrical settings were an object-to-source distance of 44.52 mm and an object-to-detector distance of 353.3 mm.

The reconstruction of the CT was done using the NRecon software (version 2.1.0.0, Bruker) based on the Feldkamp algorithm. CTAn software (version 1.18.8.0, Bruker) was used for the 3D analysis. A region of interest representative of the sample was selected and, the images were binarized. The objects of interest were represented in white color. The quantitative analyses of the sample were then performed through the 3D plug-in analysis. CTvox software (Bruker, version 3.3.0) was used for volume rendering.

Electrochemical Measurements: The electrochemical behavior was investigated in CR2032-type coin cells through galvanostatic charge-discharge measurements on a BioLogic MPG2 potentiostat, within a potential window of 1.8–2.7 V (vs Li/Li⁺). Cyclic voltammetry tests were conducted within a potential range of 1.8–2.7 V (vs Li/Li⁺) at different scanning rates, from 0.1 to 0.5 mV s⁻¹. EIS was performed using potentiostatic mode at open circuit potential. The measurements were done by applying a sinusoidal voltage with an amplitude of 5 mV and a frequency range from 100 kHz to 10 mHz.

Supporting Information

Supporting Information is available from the Wiley Online Library or from the author.

Acknowledgements

The authors acknowledge the support of Arkema for offering the PVDF-HFP, Dr. Chunzhen Yang for the Ketjen black, and Sílvia Carvalho for the CT-scan data acquisition. The SEM has been sponsored by the Ile-de-France Region in the framework of Respole, the Ile-de-France network of excellence in porous solids. W.L. acknowledges the support of the CSC scholarship (201906880002). K.O.T. acknowledges the support from the French National Research Agency: *PulsedDNP* (ANR-20-ERC9-0008) and *HFPulsedDNP* (ANR-21-CE29-0019). Financial support from the IR INFRANALYTICS FR2054 for conducting the research is gratefully acknowledged. The computational resources and services used in this work were provided by the VSC (Flemish Supercomputer Center), funded by the Research Foundation - Flanders (FWO) and the Flemish Government.

Conflict of Interest

The authors declare no conflict of interest.

Data Availability Statement

The data that support the findings of this study are openly available in ChemRxiv at <https://doi.org/10.26434/chemrxiv-2023-brbfn>, reference number 0.

Keywords

interlayers, lithium–sulfur batteries, metal–organic frameworks, mixed-matrix membranes, modeling, solid-state nuclear magnetic resonance

- [1] P. G. Bruce, S. A. Freunberger, L. J. Hardwick, J.-M. Tarascon, *Nat. Mater.* **2012**, *11*, 19.
- [2] A. Manthiram, S. H. Chung, C. Zu, *Adv. Mater.* **2015**, *27*, 1980.
- [3] G. Zhou, H. Chen, Y. Cui, *Nat. Energy* **2022**, *7*, 312.
- [4] L. Wang, W. Hua, X. Wan, Z. Feng, Z. Hu, H. Li, J. Niu, L. Wang, A. Wang, J. Liu, *Adv. Mater.* **2022**, *34*, 2110279.
- [5] H. Chen, J. Liu, X. Zhou, H. Ji, S. Liu, M. Wang, T. Qian, C. Yan, *Chem. Eng. J.* **2021**, *404*, 126470.
- [6] X. Liu, T. Qian, J. Liu, M. Wang, H. Chen, C. Yan, *Energy Storage Mater.* **2019**, *17*, 260.
- [7] Y. Huang, L. Lin, C. Zhang, L. Liu, Y. Li, Z. Qiao, J. Lin, Q. Wei, L. Wang, Q. Xie, *Adv. Sci.* **2022**, *9*, 2106004.
- [8] Z. Wang, Y. Li, H. Ji, J. Zhou, T. Qian, C. Yan, *Adv. Mater.* **2022**, *34*, 2203699.
- [9] L. P. Hou, Z. Li, N. Yao, C. X. Bi, B. Q. Li, X. Chen, X. Q. Zhang, Q. Zhang, *Adv. Mater.* **2022**, *34*, 2205284.
- [10] J. Liu, T. Qian, N. Xu, M. Wang, J. Zhou, X. Shen, C. Yan, *Energy Storage Mater.* **2020**, *24*, 265.
- [11] J. Han, S. Gao, R. Wang, K. Wang, M. Jiang, J. Yan, Q. Jin, K. Jiang, *J. Mater. Chem. A* **2020**, *8*, 6661.
- [12] Y. Zang, F. Pei, J. Huang, Z. Fu, G. Xu, X. Fang, *Adv. Energy Mater.* **2018**, *8*, 1802052.
- [13] S.-H. Chung, A. Manthiram, *J. Phys. Chem. Lett.* **2014**, *5*, 1978.
- [14] Y.-S. Su, A. Manthiram, *Nat. Commun.* **2012**, *3*, 1166.
- [15] L. Chen, H. Yu, W. Li, M. Dirican, Y. Liu, X. Zhang, *J. Mater. Chem. A* **2020**, *8*, 10709.
- [16] Y. Peng, S. Sanati, A. Morsali, H. García, *Angew. Chem.* **2023**, *135*, e202214707.
- [17] X. Ma, M. Lepoitevin, C. Serre, *Mater. Chem. Front.* **2021**, *5*, 5573.
- [18] Y. Shen, A. Tissot, C. Serre, *Chem. Sci.* **2022**, *13*, 13978.
- [19] Y. He, D. Li, L. Wu, X. Yin, X. Zhang, L. H. Patterson, J. Zhang, *Adv. Funct. Mater.* **2023**, *33*, 2212277.
- [20] Y. Zheng, S. Zheng, H. Xue, H. Pang, *J. Mater. Chem. A* **2019**, *7*, 3469.
- [21] A. E. Baumann, X. Han, M. M. Butala, V. S. Thoi, *J. Am. Chem. Soc.* **2019**, *141*, 17891.
- [22] Y. Peng, X. Wei, Y. Wang, W. Li, S. Zhang, J. Jin, *ACS Nano* **2022**, *16*, 8329.
- [23] A. Knebel, J. Caro, *Nat. Nanotechnol.* **2022**, *17*, 911.
- [24] X.-J. Hong, T.-X. Tan, Y.-K. Guo, X.-Y. Tang, J.-Y. Wang, W. Qin, Y.-P. Cai, *Nanoscale* **2018**, *10*, 2774.
- [25] J. Zhou, X. Yu, X. Fan, X. Wang, H. Li, Y. Zhang, W. Li, J. Zheng, B. Wang, X. Li, *J. Mater. Chem. A* **2015**, *3*, 8272.
- [26] W. Liu, Y. Mi, Z. Weng, Y. Zhong, Z. Wu, H. Wang, *Chem. Sci.* **2017**, *8*, 4285.
- [27] Y. Li, S. Lin, D. Wang, T. Gao, J. Song, P. Zhou, Z. Xu, Z. Yang, N. Xiao, S. Guo, *Adv. Mater.* **2020**, *32*, 1906722.
- [28] Y. Fan, Z. Niu, F. Zhang, R. Zhang, Y. Zhao, G. Lu, *ACS Omega* **2019**, *4*, 10328.
- [29] P. S. Bárcia, D. Guimarães, P. A. Mendes, J. A. Silva, V. Guillermin, H. Chevreau, C. Serre, A. E. Rodrigues, *Microporous Mesoporous Mater.* **2011**, *139*, 67.
- [30] S. Dai, C. Simms, I. Dovgaliuk, G. Patriarche, A. Tissot, T. N. Parac-Vogt, C. Serre, *Chem. Mater.* **2021**, *33*, 7057.
- [31] G. Wißmann, A. Schaate, S. Lilienthal, I. Bremer, A. M. Schneider, P. Behrens, *Microporous Mesoporous Mater.* **2012**, *152*, 64.
- [32] S. Dai, F. Nouar, S. Zhang, A. Tissot, C. Serre, *Angew. Chem.* **2021**, *133*, 4328.

- [33] H. Furukawa, F. Gandara, Y.-B. Zhang, J. Jiang, W. L. Queen, M. R. Hudson, O. M. Yaghi, *J. Am. Chem. Soc.* **2014**, *136*, 4369.
- [34] Y. Wang, Z. Deng, J. Huang, H. Li, Z. Li, X. Peng, Y. Tian, J. Lu, H. Tang, L. Chen, *Energy Storage Mater.* **2021**, *36*, 466.
- [35] X.-J. Hong, C.-L. Song, Y. Yang, H.-C. Tan, G.-H. Li, Y.-P. Cai, H. Wang, *ACS Nano* **2019**, *13*, 1923.
- [36] J. Dechnik, J. Gascon, C. J. Doonan, C. Janiak, C. J. Sumby, *Angew. Chem., Int. Ed.* **2017**, *56*, 9292.
- [37] G. Jin, J. Zhang, B. Dang, F. Wu, J. Li, *Front. Chem. Sci. Eng.* **2022**, *16*, 511.
- [38] D. K. Sannes, S. Øien-Ødegaard, E. Aunan, A. Nova, U. Olsbye, *Chem. Mater.* **2023**, *35*, 3793.
- [39] M. U. Patel, R. Demir-Cakan, M. Morcrette, J. M. Tarascon, M. Gaberscek, R. Dorninko, *ChemSusChem* **2013**, *6*, 1177.
- [40] Q. Zou, Y.-C. Lu, *J. Phys. Chem. Lett.* **2016**, *7*, 1518.
- [41] H. Wang, W. Zhang, J. Xu, Z. Guo, *Adv. Funct. Mater.* **2018**, *28*, 1707520.
- [42] C. Amerein, U. Banerjee, Z. Pang, W. Lu, V. Pimenta, K. O. Tan, *J. Magn. Reson.* **2023**, *348*, 107391.
- [43] Z. Wan, D. Lei, W. Yang, C. Liu, K. Shi, X. Hao, L. Shen, W. Lv, B. Li, Q. H. Yang, *Adv. Funct. Mater.* **2019**, *29*, 1805301.
- [44] P. Duan, J. C. Moreton, S. R. Tavares, R. Semino, G. Maurin, S. M. Cohen, K. Schmidt-Rohr, *J. Am. Chem. Soc.* **2019**, *141*, 7589.
- [45] R. Semino, J. C. Moreton, N. A. Ramsahye, S. M. Cohen, G. Maurin, *Chem. Sci.* **2018**, *9*, 315.
- [46] J. Chmiola, G. Yushin, Y. Gogotsi, C. Portet, P. Simon, P.-L. Taberna, *Science* **2006**, *313*, 1760.
- [47] W. Li, Y. Li, J. Caro, A. Huang, *J. Membr. Sci.* **2022**, *643*, 120021.
- [48] H. Xu, F. Zhong, F. Chen, T.-X. Luan, P. Li, S. Xu, J. Gao, *J. Mater. Chem. C* **2022**, *10*, 7469.
- [49] N. Widiastuti, T. Gunawan, H. Fansuri, W. N. W. Salleh, A. F. Ismail, N. Sazali, *Membranes* **2020**, *10*, 267.
- [50] W. G. Lim, C. Jo, A. Cho, J. Hwang, S. Kim, J. W. Han, J. Lee, *Adv. Mater.* **2019**, *31*, 1806547.
- [51] W. Liu, K. Zhang, L. Ma, R. Ning, Z. Chen, J. Li, Y. Yan, T. Shang, Z. Lyu, Z. Li, *Energy Storage Mater.* **2022**, *49*, 1.
- [52] Z. A. Ghazi, X. He, A. M. Khattak, N. A. Khan, B. Liang, A. Iqbal, J. Wang, H. Sin, L. Li, Z. Tang, *Adv. Mater.* **2017**, *29*, 1606817.
- [53] H. Zhang, J. Hou, Y. Hu, P. Wang, R. Ou, L. Jiang, J. Z. Liu, B. D. Freeman, A. J. Hill, H. Wang, *Sci. Adv.* **2018**, *4*, eaq0066.
- [54] Z. Chang, Y. Qiao, H. Deng, H. Yang, P. He, H. Zhou, *Joule* **2020**, *4*, 1776.
- [55] T. Lei, Y. Xie, X. Wang, S. Miao, J. Xiong, C. Yan, *Small* **2017**, *13*, 1701013.
- [56] T. Lei, W. Chen, W. Lv, J. Huang, J. Zhu, J. Chu, C. Yan, C. Wu, Y. Yan, W. He, *Joule* **2018**, *2*, 2091.
- [57] N. H. Kwon, H. Yin, T. Vavrova, J. H. Lim, U. Steiner, B. Grobóty, K. M. Fromm, *J. Power Sources* **2017**, *342*, 231.
- [58] T.-S. Chung, L. Y. Jiang, Y. Li, S. Kulprathipanja, *Prog. Polym. Sci.* **2007**, *32*, 483.
- [59] W. Li, J. Qian, T. Zhao, Y. Ye, Y. Xing, Y. Huang, L. Wei, N. Zhang, N. Chen, L. Li, *Adv. Sci.* **2019**, *6*, 1802362.
- [60] E. Barbet-Massin, A. J. Pell, J. S. Retel, L. B. Andreas, K. Jaudzems, W. T. Franks, A. J. Nieuwkoop, M. Hiller, V. Higman, P. Guerry, *J. Am. Chem. Soc.* **2014**, *136*, 12489.
- [61] G. P. Holland, T. M. Alam, *J. Magn. Reson.* **2006**, *181*, 316.
- [62] E. R. D. Azevêdo, W. Hu, T. J. Bonagamba, K. Schmidt-Rohr, *J. Am. Chem. Soc.* **1999**, *121*, 8411.
- [63] T. Gullion, J. Schaefer, *Advances in Magnetic and Optical Resonance*, Vol. 13, Elsevier, https://www.google.com/search?sca_esv=7d380bcdbd6e9b9f&sca_upv=1&rlz=1C1GCEU_enIN1078IN1078&q=Amsterdam&si=AKbGX_obynita-BNzxZrFs5Xp6xpKKQhp3e6ZAETk9w76AgBhATfr-0uD9j0WKn96jQoxUYID3IPmvUwLn2W_ZazhiO8YKrrlCUOPRG5MkaKYFwtaoDOHih64hiQ6tsQZ8RObK24Dn_XpIhkaim5c68CU4e1bMbdeHz_3v7HHod1DXvhBnlsaTGnAdrN0BWs0dxBbo7-T11Q&sa=X&ved=2ahUKEwips7Gjps2FAxUMwjgGHZ1ADwlQmxMoAXoECCYQAw, Amsterdam **1989**.
- [64] T. D. Kühne, M. Iannuzzi, M. Del Ben, V. V. Rybkin, P. Seewald, F. Stein, T. Laino, R. Z. Khaliullin, O. Schütt, F. Schiffmann, *J. Chem. Phys.* **2020**, *152*, 194103.
- [65] J. P. Perdew, K. Burke, M. Ernzerhof, *Phys. Rev. Lett.* **1996**, *77*, 3865.
- [66] S. Grimme, S. Ehrlich, L. Goerigk, *J. Comput. Chem.* **2011**, *32*, 1456.
- [67] S. Nosé, *Mol. Phys.* **1984**, *52*, 255.
- [68] S. Nosé, *J. Chem. Phys.* **1984**, *81*, 511.
- [69] G. J. Martyna, D. J. Tobias, M. L. Klein, *J. Chem. Phys.* **1994**, *101*, 4177.
- [70] J. VandeVondele, J. Hutter, *J. Chem. Phys.* **2007**, *127*, 114105.
- [71] S. Goedecker, M. Teter, J. Hutter, *Phys. Rev. B* **1996**, *54*, 1703.